Detection and Quantification of Composite Manufacturing Defects Using Guided Waves

Tyler B. Hudson[1,2], Brian W. Grimsley[3], Fuh-Gwo Yuan[1,2]

[1] North Carolina State University, Department of Mechanical and Aerospace Engineering, Raleigh, NC 27695

E-mail: tyler.b.hudson@nasa.gov, tbhudson@ncsu.edu, Tel: 1-336-817-1793

[2] National Institute of Aerospace, Hampton, VA 23666

[3] NASA Langley Research Center, Advanced Materials and Processing Branch, Hampton, Virginia 23681

ABSTRACT

A guided wave defect detection technique for cured carbon fiber reinforced polymer (CFRP) composites was investigated in this paper. This technique may be extended to perform in-process cure monitoring, defect detection and sizing, and ultimately as a closed-loop process control approach to maximize composite part quality and consistency. The predominant types of manufacturing defects associated with automated fiber placement/laminate layup followed by thermal cure include porosity, tow gaps, tow overlaps, through-the-thickness fiber waviness, and in-plane fiber waviness. The present study focused on detection methods for two classes of defects: (i) providing a metric to infer porosity formed due to variation in the matrix curing process, and (ii) imaging the overlap and gap of adjacent plies intentionally introduced during layup of the prepreg.

In the first set of experiments, three 24-ply unidirectional epoxy composite panels were manufactured such that each subsequent panel had a higher degree of cure and different values of porosity by intentionally terminating the cure cycle prematurely. The average porosity was determined by acid digestion and qualitatively confirmed by ultrasonic C-scan and optical micrographs. These panels were also investigated by guided waves. It was demonstrated that the group velocity, propagating normal to the fiber direction, of the guided waves increased monotonically from the first to the third panel. Therefore, group velocity may be utilized as a metric for degree of cure and as a means to infer porosity.

In the second set of experiments, a fully non-contact guided wave hybrid system composed of an air-coupled transducer and a laser Doppler vibrometer (LDV) was used

for imaging gap and overlap defects in adjacent tows. By transforming the transient wave response in a region covering tow gap and tow overlap from the time-space domain to the frequency-wavenumber domain, the total wavefield was separated into the incident and backscatter waves. The gap and overlap region was imaged by using a “denoised” weighted zero-lag cross-correlation (DW-ZLCC) imaging condition.

Keywords:

Non-contact inspection, Air-coupled transducer, Laser Doppler vibrometer (LDV), Frequency-wavenumber filtering, Porosity/voids, Gaps, Overlaps, Structural health monitoring (SHM), Non-destructive inspection (NDI)

Introduction

The NASA Advanced Composites Project (ACP) seeks to develop and transition technology that will reduce the timeline required by 30% for development and certification of new aircraft structure that utilizes advanced composite materials. One area of concern is the introduction of manufacturing defects in composite structural parts during various processing stages from incoming material handling, to layup, to the completion of laminate curing. Defects have detrimental effects on the quality and performance of structural parts, often leading to higher cost and significant delay in parts production and utilization.

In the composite industry, cure cycles are developed from a “trial and error” or a more effective “processing science” approach to reduce the final porosity level in the composite laminate.[1] Several studies have been published on the effects of porosity and

their detection using non-destructive inspection (NDI) techniques. Porosity is defined as a “large number of microvoids each of which is too small to be of structural significance or to be detected individually by a realistic inspection technique, but which collectively may reduce the mechanical properties of the components to an unacceptable degree.”[2] Currently, structural aerospace parts are rejected when porosity exceeds two percent by volume.[3]

Typically, porosity in composites occurs because of entrapped air, moisture, or volatile products during the curing cycle.[2] In neat resins, because of the direct effect of degree of cure on the modulus of the resin, degree of cure has been inferred from ultrasonic velocity (Frequencies in the low MHz range).[4,5,6] In carbon fiber reinforced polymer (CFRP), it has been shown that as the porosity level increases, the ultrasonic velocity of the wave propagating through-the-thickness decreases.[7] The time delay between the pulse and echo of an ultrasound transducer plateaus (i.e., the ultrasonic velocity ceases to increase) during the cure cycle near the completion of cure (e.g., in graphite/epoxy composites,[8] and epoxy matrices[9]). Non-contact, air-coupled transducers can be used for ultrasonic velocity measurement in resins when direct line of sight to the resin is available during curing (i.e., no caul plate, breather cloth, vacuum bag, etc.).[10] Using piezoceramic actuators and sensors mounted directly to the mold can alleviate the unreliable coupling observed between a traditional contact ultrasound transducer and the mold which occurs most often during the heating and cooling phases.[11] Other ultrasonic phenomena have also been used for monitoring degree of cure including attenuation,[2,6,7,8,12] instantaneous phase,[13] and the “mean value of each frequency curve weighted by the maximum corresponding spectral amplitude.”[13]

Based on the premise that the level of porosity may be dictated by the change of the ultrasonic wave speed, this work examined the group velocity of guided waves in several panels with different degrees of cure and levels of porosity. The significance of this approach was that unlike conventional ultrasound that provides information about the quality of the part directly underneath or near the ultrasonic transducer in a point-by-point (discrete) inspection, the guided wave approach interrogated a continuous wave path through the thickness of the panel along the line from actuator to sensor. Thus, this yielded an "averaged" velocity in the region along the line traveled, in contrast to the point-by-point bulk velocity measurement. In addition, the experiment was designed such that it may be transitioned into a real-time detection system during cure. If the level of porosity can be determined during cure, the cure cycle can be adaptively adjusted based on the real-time and in-situ measurements. This would prevent the human operator from having to strictly follow a prescribed or non-optimized cure cycle.

There has been significant advancements in using automated fiber placement (AFP) to fabricate large scale commercial composite structures for aerospace applications. Through automated processes, more consistent quality and cost-effective manufacture of advanced composite structures are achieved. Even though the manufacture is fully autonomous, the AFP processes inevitably introduce defects.[14] Ply gaps and overlaps occur primarily at tow boundaries during the layup process near curved contour regions and can further lead to surface waviness.[15] Their effect of generating local stress concentrations on the ultimate strengths of composite laminates has been experimentally investigated.[16] Several optical imaging techniques have been or are being developed for the detection of gaps and overlaps during layup from an AFP machine. The detection

system can be manual, semi-, or fully automated.[15,17,18,19] Recently, a robotic laser scanning system has been proposed to image the gap and overlap regions during the tow laying process.[19] Eddy currents have shown initial promise for the detection of gaps and overlaps on uncured prepreg in a controlled research environment.[20] However, none of these systems are capable of detecting gaps and overlaps missed during layup in a panel that has already been cured.

For this study, an image of the gap and overlap regions was devised by a fully non-contact laser ultrasound system based on a guided wave-based approach. The system was composed of a stationary air-coupled transducer, operating in the vicinity of the gap and overlap region, and a laser Doppler vibrometer (LDV) that captured the wavefield by scanning the region. The wavefield, in time series, was then transformed into the frequency-wavenumber domain. In this domain, the incident and backscatter wavefields can be readily separated. Frequency-wavenumber filtering has previously been used for improved damage imaging of longitudinal slits in aluminum plates,[21,22,23] disbonding in a composite wing,[24] delamination in a multi-layer composite plate,[24] and local zones of high porosity/voids.[25] The imaging metrics utilized were the root mean square distribution of the reflected signal,[21] cumulative standing wave energy,[22] zero-lag cross-correlation (ZLCC),[23] standing wave filter,[24] Laplacian image filter,[24] and “denoised” weighted zero-lag cross-correlation (DW-ZLCC).[25] For this work, the DW-ZLCC imaging condition previously implemented for local zones of high porosity/voids was utilized to reveal and image the gap and overlap region.

Experimentation

Porosity Detection

Three panels of twenty-four ply unidirectional Hexcel® IM7/8552 prepreg were fabricated in a vacuum press according to the cure cycles shown in Figure 1. The unidirectional panels were 305 mm × 305 mm with nominal thickness of 3 mm. Apart from the third panel which is fully cured, the first two panels were partially cured. The transformation of the resin from the liquid to rubbery state is typically referred to as gelation. The subsequent transformation from the rubbery state to the glass state is defined as vitrification.[26] The cure cycle for the first panel was terminated prior to gelation, the second prior to vitrification.[27] Therefore, each subsequent panel had a higher degree of cure than the previous one based on the temperature cycle experienced during the cure, also shown in Figure 1. It should be noted that Panels #1 and #2 solidify during cooldown. All panels were tested in their solid state upon completion of their respective cure cycle.

Insert Figure 1

Figure 1. Cure cycle for Panel #1, #2, and #3.

After cure, each of the three panels was C-scanned with a Sonix, Inc. immersion ultrasound system in pulse-echo mode measuring amplitude using a Panametrics 15 MHz transducer. After C-scan, the panels were examined by the guided wave approach. A guided wave was excited into the plate using a five-cycle, Hanning windowed sinusoidal toneburst signal with a center frequency of 300 kHz emitted from a waveform generator (Agilent Technologies: 81150A) to an amplifier (Krohn-Hite Corporation: Model 7602M) to a piezoelectric disc (Steiner and Martins Inc.: SMD07T02R412WL). The

plate response was recorded by another piezoelectric disc in a pitch-catch configuration (Figure 2). To propose a metric or measure for porosity in the matrix, wave propagation normal to the fiber direction of the plate (i.e., 90 degree direction), which is matrix dominated, was measured. Each of the piezoelectric discs in the bottom row served as an actuator (Figure 3). Note that normal to fiber direction (90 degree direction) refers to *y*-axis and not through-the-thickness of the plate. The plate response was recorded by the three piezoelectric discs along the same vertical column. This process was repeated for each of the four columns giving a total of twelve measurements.

Insert Figure 2

Figure 2. Experimental setup for detecting porosity level related to the ultrasonic wave velocity of a 24-ply unidirectional composite using piezolelectric discs.

Inser Figure 3

Figure 3. Actuation and sensing locations normal to the fiber (ninety degree) direction.

Following the guided wave testing, photo-microscopy imaging was performed. Two 76.2 mm × 19.1 mm specimens were obtained from each fabricated panel using a diamond-abraded wet-saw. The cut surfaces were polished to a mirror finish using varying grit paper. The consolidation quality of the carbon fiber reinforced polymer was observed utilizing a digital light-microscope at 100X magnification.

In order to determine the average fiber volume fraction (FVF) and void volume fraction (VVF) of the fabricated panels, six 19.1 mm x 19.1 mm specimens were obtained from various regions of each of the panels. After determining the mass and density of the specimens according to ASTM D792, the FVF and VVF were determined following

ASTM D3171, Procedure B-Matrix digestion using a mixture of sulfuric acid and hydrogen peroxide. The specimens obtained from the panel weighed 0.789g to 0.836g.

Gap and Overlap Detection

An additional panel was laid up by hand using the same Hexcel® IM7/8552 unidirectional prepreg. The layup was [0_4/90/90_2/90/0_4] where a pair of gap and overlap defects were intentionally introduced between adjacent prepreg strips. The gap and overlap defects were located at the two plies in the middle symmetric plane. The entire panel was 150.4 mm × 150.4 mm × 1.524 mm (nominal) [6 in. × 6 in. × 0.06 in. (nominal)] and the long overlap and the gap regions were of dimensions 63.5 mm × 6.35 mm × 0.25 mm (2.5 in × 0.25 in. × 0.01 in.) (Figure 4). The panel was cured in a vacuum press following the cure cycle recommended by Hexcel®. The temperature and pressure scheme for the cure cycle was similar to that of Panel #3 in Figure 1.

Insert Figure 4

Figure 4. Layup of panel with intentionally introduced gap and overlap defects near the neutral ply surface of the composite laminate.

An unfocused circular air-coupled transducer with an active diameter of 25 mm (Ultran Group: NCG200-D25) was used to excite a five-cycle, Hanning windowed sinusoidal toneburst acoustic wave with a center frequency of 250 kHz. The air-coupled transducer was placed approximately 35 mm normal from the plate (Figure 5). At this distance, the beam width was about the width of the active diameter of the transducer resulting in an ellipse shaped excitation area on the plate of approximately 25.7 mm × 25 mm. The ellipse shape was due to the inclined angle of the transducer toward the plate. The

location of the air-coupled transducer was stationary while the out-of-plane velocity of the A_0 Lamb wave mode was recorded in a 1 mm × 1 mm grid inside a scan area (37 mm × 39 mm) located in front of the ACT (Figure 6) by a LDV (Polytec Inc.: OFV-505) (Figure 5). After each scan, the ACT and the scan area was moved up 10 mm and the scan repeated. This was done with the ACT excitation both to the right and to the left of the region containing the gap and the overlap a total of eighteen times (nine on each side). For the eighteen scans, the ACT was centered approximately at y = 27 mm to y = 107 mm at increments of 10 mm. The beginning and ending x coordinates were x = 72 mm to x = 109 mm for all but two scans (these were shifted slightly to the right) (Figure 6).

Inert Figure 5

Figure 5. Experimental setup for detecting gap and overlap regions.

Insert Figure 6

Figure 6. Excitation locations of air-coupled transducer and total LDV scan area from all scans.

Results and Discussion

Porosity Detection

The group velocity of the guided wave, c_g, was calculated as the distance between the center of the actuator and the center of the sensor, $d_{a\text{-}s}$, divided by the time of arrival (TOA) [Eq. (1)]

$$c_g = \frac{d_{a-s}}{t_s - t_a} \tag{1}$$

where t_a is the time of actuation (as determined by the oscilloscope) and t_s is the time of arrival at the sensor.

Using the TOA instead of the time difference of arrival (TDOA) between a pair of sensors gives an additional group velocity measurement. For instance, one actuator and three sensors results in three independent group velocity calculations whereas three sensor measurements alone results in two independent group velocity calculations. TDOA between a pair of sensors to calculate group velocity has been often used (e.g., Kishimoto et al.[28] and Jeong et al.[29]). A key assumption enabling the use of the TOA method was that there was negligible difference in the time it takes for the input voltage to transmit from the waveform generator to channel one of the oscilloscope compared to the travel time from waveform generator through the amplifier to the actuator. A BNC (Bayonet Neill–Concelman) splitter was placed on the output of the waveform generator (Figure 2) creating two travel paths for the input voltage: (1) to channel one of the oscilloscope and (2) through the amplifier to the actuator. This paper assumes that any error of this assumption was justified by the additional group velocity measurements it provided. A higher *n*-value (number of independent group velocity measurements) reduces the error from standard deviation.

To determine t_a and t_s, the following algorithm was implemented. First, the time at which there is minimum response was determined and recorded as $t_{a(s)}|_{\min}$. Then, the time at the maximum peak prior to $t_{a(s)}|_{\min}$ was determined and recorded as $t_{a(s)}|_{\max}$. The reason $t_{a(s)}|_{\max}$ must be prior to $t_{a(s)}|_{\min}$ was that the asymmetric five-cycle toneburst signal

generated was defined where the minimum value occurs after the maximum (Figure 7). $t_{a(s)}|_{\min}$ and $t_{a(s)}|_{\max}$ were checked to ensure that they occur on subsequent peaks by Eq. (2). If $t_{a(s)}|_{\min}$ and $t_{a(s)}|_{\max}$ did not satisfy Eq. (2), a secondary algorithm must be implemented to determine $t_{a(s)}|_{\max}$.

$$\frac{t_{a(s)}\Big|_{\min} - t_{a(s)}\Big|_{\max}}{N / f_c} \leq 1 \tag{2}$$

where N equals the number of peaks which is five for this excitation signal and f_c is the center frequency (300 kHz).

For each of the twelve measurements, $t_{a(s)}|_{\min}$ and $t_{a(s)}|_{\max}$ did satisfy Eq. (2). $t_{a(s)}$ was then calculated as the average of $t_{a(s)}|_{\min}$ and $t_{a(s)}|_{\max}$ [Eq. (3)].

$$t_{a(s)} = \frac{t_{a(s)}\Big|_{\min} + t_{a(s)}\Big|_{\max}}{2} \tag{3}$$

A plot of the actuation waveform and one of the sensor responses with the key time points in the algorithm is shown in Figure 7.

Insert Figure 7

Figure 7. Actuation waveform (five-cycle, Hanning windowed sinusoidal toneburst signal with a center frequency of 300 kHz) and plate response from sensor located 127 mm from actuator.

The average group velocity was then determined from the group velocities of each of the twelve actuator-sensor pairs. The three points in Figure 8 correspond to the average group velocity of each of the three panels. The cure time value (x-axis) is denoted by the time at which the composite panel began to cool during the curing cycle (Figure 1). The

error bars show the variation based on a 90% confidence interval of the twelve measurements. The average group velocity increased by 5.52 percent from Panel #1 to Panel #2 and another 1.26 percent from Panel #2 to Panel #3 (Figure 8).

Insert Figure 8

Figure 8. Group velocity normal to the fiber direction on each of three panels of varying final degrees of cure (Actuation with 300 kHz center frequency).

With longer cure times, each subsequent panel had a higher degree of cure. As a qualitative measure of porosity, the C-scan results (Figure 9) and micrographs (Figure 10) showed a decrease in the number of voids between Panel #1 and Panel #2 and a negligible difference between Panel #2 and Panel #3. In the C-scan results, yellow is the lowest amplitude (indicative of voids) and purple is the highest amplitude.

Insert Figure 9

Figure 9. C-scan images of fabricated panels: (a) Panel #1, (b) Panel #2, and (c) Panel #3.

Insert Figure 10

Figure 10. Micrographs at two locations in (a) Panel #1, (b) Panel #2, and (c) Panel #3.

As a quantitative measure of porosity, acid digestion confirmed the results of both the C-scan and micrographs. Panel #1 had an average porosity of 2.06% (Range: 1.06% to 4.52%) from the six samples tested, Panel #2 had an average porosity of 0.14% (Range: 0.03% to 0.44%) from the six samples tested, and Panel #3 had an average porosity of 0.18% (Range: 0.01% to 0.48%) from the six samples tested (Volume Fraction of Voids, Table 1). It should be noted that Panel #2 and Panel #3 did not have a significantly different value of porosity considering the range in acid digestion measurements.

Table 1. Acid digestion results for Panel #1, #2, and #3.

		Panel #1	Panel #2	Panel #3
Specimen Initial Mass (g)	Average	0.8165	0.8032	0.8032
	Min	0.7901	0.7893	0.7986
	Max	0.8360	0.8205	0.8083
Specimen Density (g/ml)	Average	1.5507	1.5995	1.5971
	Min	1.5089	1.5930	1.5945
	Max	1.5793	1.6053	1.6037
Volume Fraction of Fiber (%)	Average	58.90	62.77	62.37
	Min	53.36	61.46	61.39
	Max	62.88	64.11	64.29
Volume Fraction of Voids (%)	Average	2.46	0.14	0.18
	Min	1.46	0.03	0.01
	Max	4.52	0.44	0.48

The average group velocity increased monotonically from Panel #1 to Panel #3 with the greatest increase between Panel #1 and Panel #2. Therefore, preliminary results indicate

that the group velocity of a guided wave could possibly be used as an initial index (or metric) to determine the degree of cure, and infer the level of porosity. The slight increase in group velocity between Panel #2 and Panel #3 could be associated with increased degree of cure. This methodology is being transitioned into an in-situ detection system that will be capable of real-time monitoring of the degree of cure and porosity in a laminate during autoclave or oven cure. The system will then consist of high temperature actuators and sensors that can withstand the temperature and pressure during cure and high temperature cables that will connect the actuators and sensors to the electronics located outside the cure environment. Additional metrics such as attenuation of wave energy, which will play a critical role during the early stages of cure when the resin is in the liquid state, will be investigated

Gap and Overlap Detection

After the gap/overlap panel was cured it was removed from the mold and C-scanned with the same system described previously to establish a baseline to compare with the guided wave approach (Figure 6). Again, yellow is the lowest amplitude (indicative of the defect) and purple is the highest amplitude. The scan area location shown in Figure 6 is also shown in Figure 11 for reference.

Insert Figure 11

Figure 11. C-scan image of panel with intentionally introduced overlap and gap.

For the guided wave approach, the angle of incidence of the air-coupled transducer was set to 13.5 degrees from normal direction of the plate. This value was optimized to ensure maximum amplitude of the desired A_0 mode of the propagating wave in the

plate.[30] The optimum angle was determined from the phase velocity dispersion curve (Figure 12).

Insert Figure 12

Figure 12. Phase velocity dispersion curve for the [0_4/90/90_2/90/0_4] composite plate.

At the center frequency of the excited wave (250 kHz), two fundamental wave modes simultaneously exist (A_0 and S_0). A_0 and S_0 are the antisymmetric and symmetric zero-order Lamb wave modes, respectively. Since the magnitude of the transverse velocity generated by the S_0 mode is much smaller than the A_0 mode, the S_0 mode captured by the LDV is much less sensitive. Therefore, in this study only the A_0 mode was chosen for processing the wave signals. At 250 kHz, the phase velocity of the A_0 mode is 1.452 km/s. Using Eq. (4),[30] the optimal angle of excitation, θ, was calculated

$$\sin\theta = \frac{c}{c_p} \tag{4}$$

where c is the sound velocity in the excitation medium (Air: 343 m/s) and c_p is the phase velocity of the A_0 mode in the plate (1.452 km/s). The resulting optimal angle of excitation for the air-coupled transducer was 13.66 degrees (13.5 degrees was used in the experiment).

As the plate was excited from the air-coupled transducer, Lamb waves were generated and then propagated in the plate. The out-of-plane velocity of the wavefield, defined by $w(x, y, t)$, was assembled from all the time series captured by the LDV from each scan. The wavefield was then windowed in time after the actuation is triggered, and prior to the wave reflected back from opposite edge of the plate. Each time trace of the wavefield

$w(x, y, t)$ was "denoised" at every measurement location (x_i, y_j) using a one-dimensional wavelet transform. After "denoising" in the time domain, the noise was further mitigated in the space domain at every time snapshot using a two-dimensional wavelet transform. The wavelet utilized was the Daubechies wavelet (db10) with five levels of decomposition. At each decomposition level, MatLab's Stationary Wavelet Transform Denoising application was used to calculate the threshold values.[31] The preprocessed wavefield $w(x, y, t)$ is plotted at several time steps as a 2-D contour plot for the scan where the ACT is centered at y = 20 mm and on the left of the scan area (Figure 13).

Insert Figure 13

Figure 13. 2-D contour plots of the out-of-plane velocity, $w(x, y, t)$, of wavefield at times (a) 242 μs, (b) 252 μs, (c) 261 μs, and (d) 271 μs for the scan where the ACT is centered at y = 20 mm and on the left of the scan area.

The DW-ZLCC imaging condition for imaging the defect is based on the concept that the incident and backscattered wave are in phase on the damage boundaries.[25] When the incident wavefield interacts with the overlap, the backscattered wavefield was generated. At the instant of the wave reflection at an arbitrary location of the defect zone, the two wavefields propagating in different directions are coherent or in phase. To decompose $w(x, y, t)$ into the incident and backscatter wave, $w(x, y, t)$ was first transformed from the time-space domain to the frequency-wavenumber domain.[22] This can be accomplished using a two-dimensional Fourier transform [Eq. (5)].

$$\bar{W}(k_x, y, \omega) = \int_{-\infty}^{\infty} \int_{-\infty}^{\infty} w(x, y, t) \mathrm{e}^{-i(k_x x - \omega t)} \, \mathrm{d}x \, \mathrm{d}t \tag{5}$$

The total wavefield can be readily separated in the frequency-wavenumber domain into the incident $\bar{W}_i(k_x, y, \omega)$ and the backscatter $\bar{W}_{bs}(k_x, y, \omega)$ wave based on the sign of k_x. Both the incident wave and the backscattered wave were inverted to the frequency-space domain using a one-dimensional spatial Fourier transform [Eq. (6)].

$$W_{i(bs)}(x, y, \omega) = \frac{1}{2\pi}\int_{-\infty}^{\infty} \bar{W}_{i(bs)}(k_x, y, \omega)\, \mathrm{e}^{ik_x x}\mathrm{d}x \tag{6}$$

To ensure that the imaging condition applied was independent of distance from the ACT, a weighting factor was applied to the incident wavefield which attenuates with propagation distance from area of excitation. The weighting factor was based on the cumulative total wave energy (CTWE). The CTWE can be calculated by

$$CTWE(x, y) = \int_{t_i}^{t_f} w^2(x, y, t)\ \mathrm{d}t \tag{7}$$

where t_i is the time at the beginning of the time window measurement and t_f is the time at the end of the time window (prior to the back reflection from the edge of the plate).[22] After calculating the CTWE at each measurement location (x_i, y_j), the CTWE is averaged across each x-coordinate [Eq. (8)].

$$\overline{CTWE}(x_i) = \sum_{j=1}^{m} CTWE(x_i, y_j)/m \tag{8}$$

A custom 1-D curve equation [Eq. (9)] was fit to the $\overline{CTWE}(x_i)$ data using the curve fitting toolbox in MatLab[32] to define the weight function.

$$A_{CTWE}(x) = Be^{-2\alpha(x-x_0)} \tag{9}$$

where x_0 is the x-coordinate of the ACT, B is the estimated amplitude at x_0, and α is the attenuation factor. A more detailed explanation of the theory behind this weighting factor can be found in Hudson et al.[25]

The incident wave in the frequency-space domain, $W_i(x_i, y_j, \omega_k)$, was weighted [Eq. (10)] by the curve fitted to the average CTWE at each *x*-coordinate.

$$W_{i,CTWE}(x_i, y_j, \omega_k) = W_i(x_i, y_j, \omega_k) \big/ A_{CTWE}(x_i) \tag{10}$$

The weighted incident wave was then used to determine the DW-ZLCC, $I_{CTWE}(x_i, y_j)$, at each measurement location (x_i, y_j) using Eq. (11).

$$I_{CTWE}(x_i, y_j) = \sum_{\omega} W_{i,CTWE}(x_i, y_j, \omega_k) W^*_{bs}(x_i, y_j, \omega_k) \tag{11}$$

By weighting the incident wavefield, the intensity, $I_{CTWE}(x_i, y_j)$, was independent of distance from excitation. As an incremental step in Eq. (11), $I_{CTWE}(x_i, y_j)$ was calculated with noise removal at each ω_k step before summation. As before, the noise was mitigated by using a two-dimensional wavelet transform (Daubechies 10 level 5) in the space domain and the horizontal, vertical, and diagonal thresholds were calculated using MatLab's wavelet toolbox.[31]

After $I_{CTWE}(x_i, y_j)$ was calculated for each scan, the results were superimposed to form a single image. Figure 14a shows the standard ZLCC imaging condition and Figure 14b shows the DW-ZLCC imaging condition for the total scan area. The gap and overlap locations are denoted by a dashed outline. The distinct improvement of the DW-ZLCC imaging condition can be observed by comparison of Figure 14b (DW-ZLCC) with Figure 14a (ZLCC). The standard ZLCC imaging condition does not "denoise" or weight the incident wave.

Insert Figure 14

Figure 14. (a) ZLCC and (b) DW-ZLCC imaging condition [Gap (top) and overlap (bottom) locations are denoted by a dashed outline].

The accuracy of the result is limited by the following factors. First, to achieve sufficient power, the actuation frequency was limited to a range near the resonant frequency of the ACT. If a higher frequency could be measured, then the propagating wave would have a smaller wavelength leading to a greater interaction with the gap and overlap. In addition, only a single center frequency was used in the test. Other center frequencies or a chirp actuation waveform could be used and the results superimposed to provide greater accuracy. Lastly, the A_0 mode is a flexural mode; therefore, the stress is at a minimum at the neutral axis of the plate. This causes the wave interaction with the gap and overlap to be minimized when the overlap location is at the center of the plate compared to any other location through the thickness. This is a "worst-case" location through the thickness in terms of being able to detect it with this methodology.

The future work concerning this detection system will be to mitigate/modify these factors to sharpen the image within the constraints of the equipment. The technique has been extended from the detection and size determination of local zones of high porosity/voids[25] to gaps and overlaps and has the potential to image other composite manufacturing defects including through-the-thickness fiber waviness, and in-plane fiber waviness.

Summary of Results and Conclusions

In this paper, two classes of manufactured defects, overall porosity and gap/overlap regions, are quantified and imaged respectively, using a guided wave approach. For

providing a metric related to degree of cure and inferring overall porosity, three 24-ply unidirectional composite panels were fabricated using a vacuum press where each subsequent panel had a higher final degree of cure than the previous one by prematurely terminating the cure cycle. Guided waves were propagated and recorded in a pitch-catch configuration normal to the fiber direction using piezoelectric actuators and sensors. From the group velocity calculated from the TOA of the actuator-sensor pairs, the average group velocity was determined. The average group velocity of the guided waves increased by 5.52 percent from the first panel to the second panel and 1.26 percent from the second panel to the third. Acid digestion found that Panel #1, Panel #2, and Panel #3 had an average porosity of 2.06% (Range: 1.06% to 4.52%), 0.14% (Range: 0.03% to 0.44%), and 0.18% (Range: 0.01% to 0.48%), respectively, from the six samples tested in each panel confirming the qualitative results of both C-scan results and micrographs. Thus, the group velocity of a guided wave may have the potential to serve as an initial index for estimating the degree of cure and level of porosity with further work. The slight increase in group velocity observed between Panel #2 and Panel #3 is likely associated with increased degree of cure.

An additional composite panel with an intentionally introduced gap and overlap in the middle two layers was cured in a vacuum press. For imaging the gap/overlap regions, a stationary unfocused air-coupled transducer excited a guided wave in the composite plate and a LDV recorded the out-of-plane velocity of the plate. The response was transformed from the time-space domain to the frequency-wavenumber domain and then separated into the incident and backscatter wave. The DW-ZLCC imaging condition was proposed to image the gap and overlap regions where the incident and backscattered

waves were in phase. The image produced from the guided wave approach did not provide an explicitly clear image (full location not identified) for both the gap and the overlap. The image of the gap region was clearer than the overlap region, perhaps due to entrapped air in the gap having greater interaction with the wave than the additional fibers of the overlap. However, it was of similar resolution to that of immersion C-scan even with much larger wavelength and non-contact inspection. The DW-ZLCC unequivocally outperformed the standard ZLCC imaging condition.

Acknowledgement

The authors would like to acknowledge the financial support from a Graduate Research Assistantship at National Institute of Aerospace through the Advanced Composites Project (Fund Code: AERX22017D) at NASA Langley Research Center (Contract: NNL09AA00A).

References

1. Hou TH. Cure cycle design methodology for fabricating reactive resin matrix fiber reinforced composites: A protocol for producing void-free quality laminates. *NASA TM 2014-218524* 2014: 1-16.
2. Birt E and Smith R. A review of NDE methods for porosity measurement in fibre-reinforced polymer composites. *Insight-Non-Destructive Testing and Condition Monitoring* 2004; 46(11): 681-686.

3. Kaufmann M, Zenkert D and Mattei C. Cost optimization of composite aircraft structures including variable laminate qualities. *Composites Science and Technology* 2008; 68(13): 2748-2754.

4. Lindrose AM. Ultrasonic wave and moduli changes in a curing epoxy resin. *Experimental Mechanics* 1978; 18(6): 227-232.

5. Speake J, Arridge R and Curtis G. Measurement of the cure of resins by ultrasonic techniques. *Journal of Physics D: Applied Physics* 1974; 7(3): 412-424.

6. Adams R and Cawley P. A review of defect types and nondestructive testing techniques for composites and bonded joints. *NDT International* 1988; 21(4): 208-222.

7. Stone D and Clarke B. Ultrasonic attenuation as a measure of void content in carbon-fibre reinforced plastics. *Non-Destructive Testing* 1975; 8(3): 137-145.

8. Chen J, Hoa S, Jen C and Wang H. Fiber-optic and ultrasonic measurements for in-situ cure monitoring of graphite/epoxy composites. *Journal of Composite Materials* 1999; 33(20): 1860-1881.

9. Maffezzoli A, Quarta E, Luprano V, Montagna G and Nicolais L. Cure monitoring of epoxy matrices for composites by ultrasonic wave propagation. *Journal of Applied Polymer Science* 1999; 73(10): 1969-1977.

10. Lionetto F, Tarzia A and Maffezzoli A. Air-coupled ultrasound: a novel technique for monitoring the curing of thermosetting matrices. *IEEE Transactions on Ultrasonics, Ferroelectrics and Frequency Control* 2007; 54(7): 1437-1444.

11. Liebers N, Raddatz F and Schadow F (2013) *Effective and Flexible Ultrasound Sensors for Cure Monitoring for Industrial Composite Production.* : Deutsche Gesellschaft für Luft-und Raumfahrt-Lilienthal-Oberth eV.

12. Jeong H and Hsu D. Experimental analysis of porosity-induced ultrasonic attenuation and velocity change in carbon composites. *Ultrasonics* 1995; 33(3): 195-203.

13. Pavlopoulou S, Soutis C and Staszewski W. Cure monitoring through time-frequency analysis of guided ultrasonic waves. *Plastics, Rubber and Composites* 2012; 41(4-5): 4-5.

14. Dirk HL, Ward C and Potter KD. The engineering aspects of automated prepreg layup: History, present and future. *Composites Part B: Engineering* 2012; 43(3): 997-1009.

15. Louie M and Yuan FG. Composite defects from automated fiber placement. Masters of Mechanical Engineering Final Project, North Carolina State University: Raleigh, NC. 2014.

16. Croft K, Lessard L, Pasini D, Hojjati M, Chen J and Yousefpour A. Experimental study of the effect of automated fiber placement induced defects on performance of composite laminates. *Composites Part A: Applied Science and Manufacturing* 2011; 42(5): 484-491.

17. Rudberg T and Cemenska J. Incorporation of laser projectors in machine cell controller reduces ply boundary inspection time, on-part course identification and part probing. *SAE Int.J.Aerosp* 2012; 5(1): 74-78.

18. Belhaj M, Deleglise M, Comas-Cardona S, Demouveau H, Binetruy C, Duval C, et al. Dry fiber automated placement of carbon fibrous preforms. *Composites Part B: Engineering* 2013; 50: 107-111.

19. Maass DP. Development of a testbed for automated ply inspection of composites. *Proceedings SAMPE Technical Conference, Baltimore, MD* 2015: 123-139.

20. Schmidt C, Schultz C, Weber P and Denkena B. Evaluation of eddy current testing for quality assurance and process monitoring of automated fiber placement. *Composites Part B: Engineering* 2014; 56: 109-116.

21. Ruzzene M. Frequency–wavenumber domain filtering for improved damage visualization. *Smart Materials and Structures* 2007; 16(6): 2116-2129.

22. An Y, Park B and Sohn H. Complete noncontact laser ultrasonic imaging for automated crack visualization in a plate. *Smart Materials and Structures* 2013; 22(2): 025022.

23. Zhu R, Huang G and Yuan FG. Fast damage imaging using the time-reversal technique in the frequency–wavenumber domain. *Smart Materials and Structures* 2013; 22(7): 075028.

24. Sohn H, Park G, Wait JR, Limback NP and Farrar CR. Wavelet-based active sensing for delamination detection in composite structures. *Smart Materials and Structures* 2004; 13(1): 153-160.

25. Hudson TB, Hou T, Grimsley BW and Yuan F. Imaging of local porosity/voids using a fully non-contact air-coupled transducer and laser Doppler vibrometer system. *Structural Health Monitoring* 2016; 16: 164-173.

26. Farquharson S, Carignan J, Khitrov V, Senador A and Shaw M. Development of a phase diagram to control composite manufacturing using Raman spectroscopy. *Proceedings SPIE 5272, Industrial and Highway Sensors Technology,* 2004: 19-29.

27. Hudson TB, Grimsley BW and Yuan FG. Development of a fully automated guided wave system for in-process cure monitoring of CFRP composite laminates. *Proceedings of the American Society for Composites: Thirty-First Technical Conference, Williamsburg, VA* 2016.

28. Kishimoto K, Inoue H, Hamada M and Shibuya T. Time frequency analysis of dispersive waves by means of wavelet transform. *Journal of Applied Mechanics* 1995; 62(4): 841-846.

29. Jeong H. Analysis of plate wave propagation in anisotropic laminates using a wavelet transform. *NDT & E International* 2001; 34(3): 185-190.

30. Harb MS and Yuan FG. A rapid, fully non-contact, hybrid system for generating Lamb wave dispersion curves. *Ultrasonics* 2015; 61: 62-70.

31. *MATLAB and Wavelet Toolbox Release 2015a, the MathWorks, Inc., Natick, Massachusetts, United States.*

32. *MATLAB and Curve Fitting Toolbox Release 2015a, The MathWorks, Inc., Natick, Massachusetts, United States.*

Figures

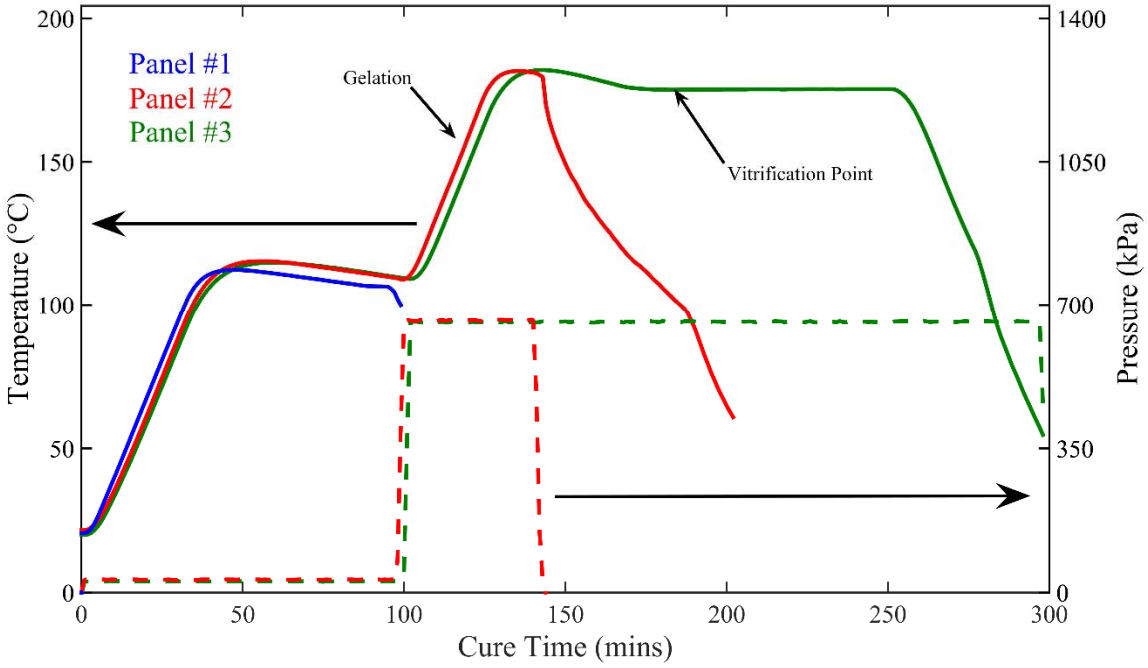

Figure 1. Cure cycle for Panel #1, #2, and #3.

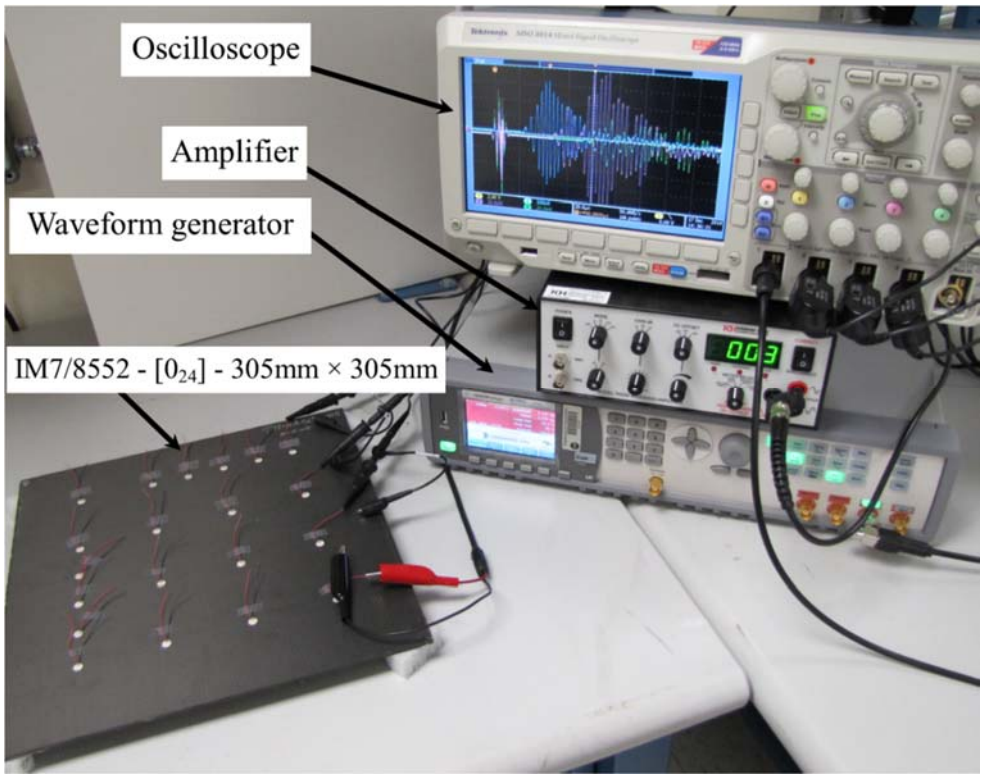

Figure 2. Experimental setup for detecting porosity level related to the ultrasonic wave velocity of a 24-ply unidirectional composite using piezolelectric discs.

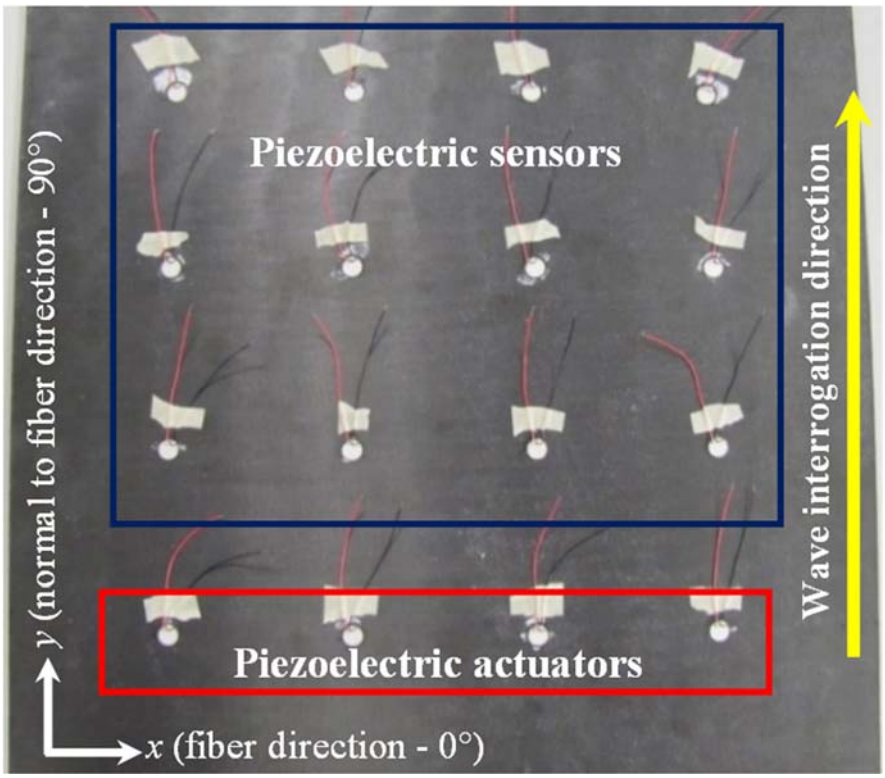

Figure 3. Actuation and sensing locations normal to the fiber (ninety degree) direction.

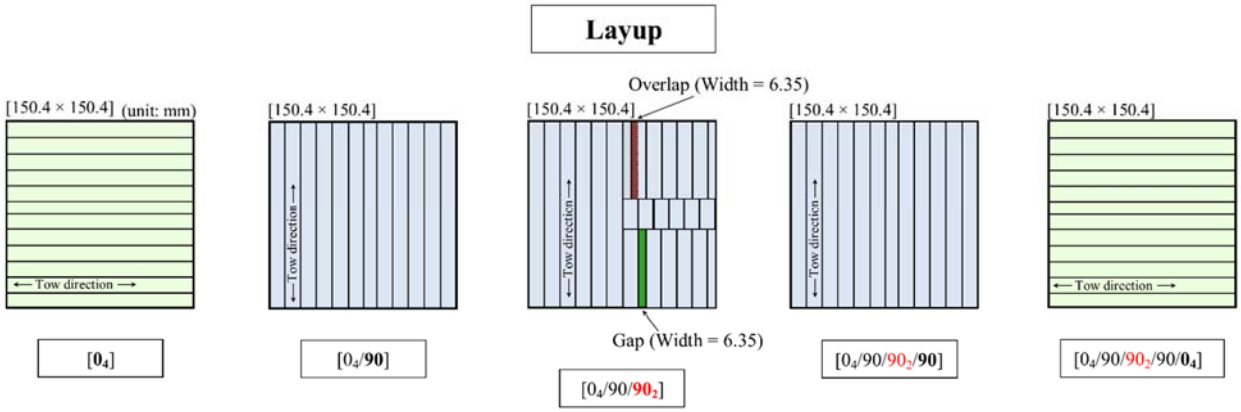

Figure 4. Layup of panel with intentionally introduced gap and overlap defects near the neutral ply surface of the composite laminate.

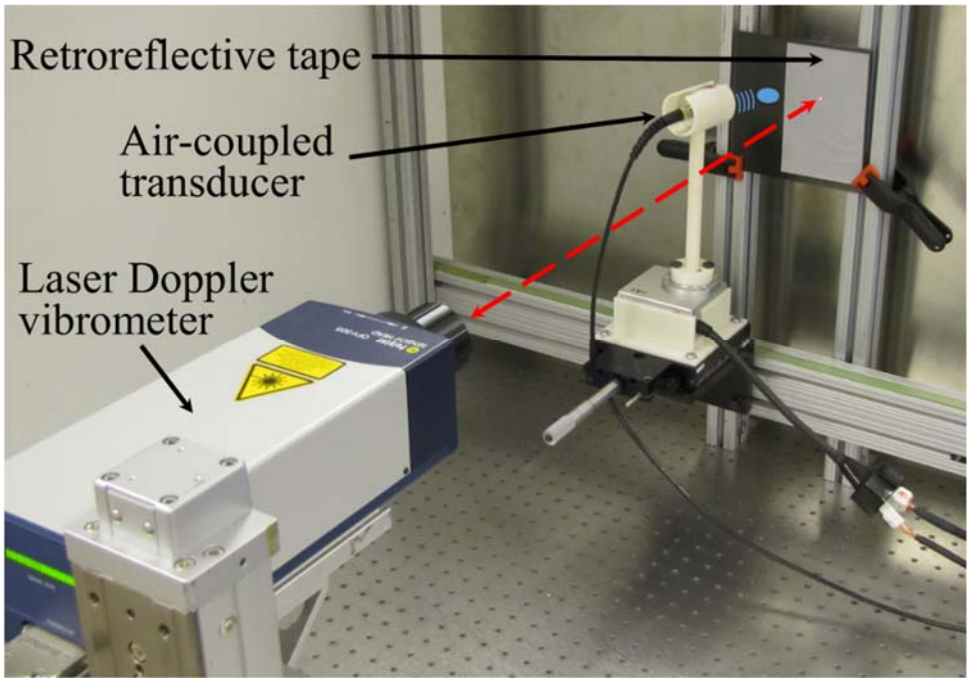

Figure 5. Experimental setup for detecting gap and overlap regions.

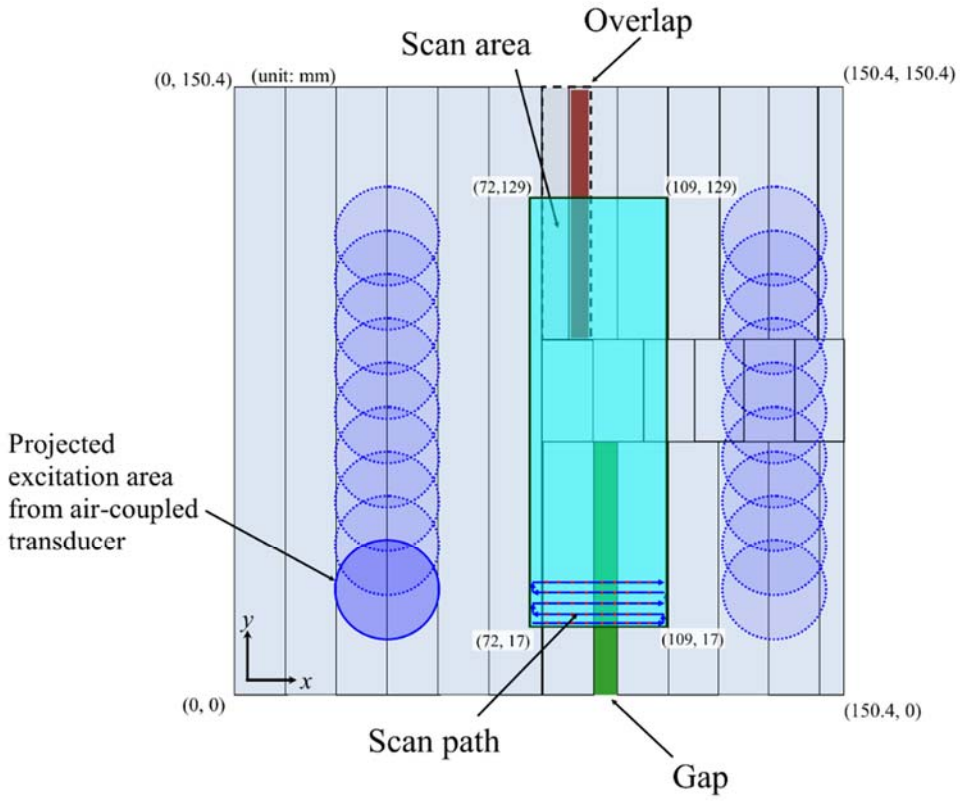

Figure 6. Excitation locations of air-coupled transducer and total LDV scan area from all scans.

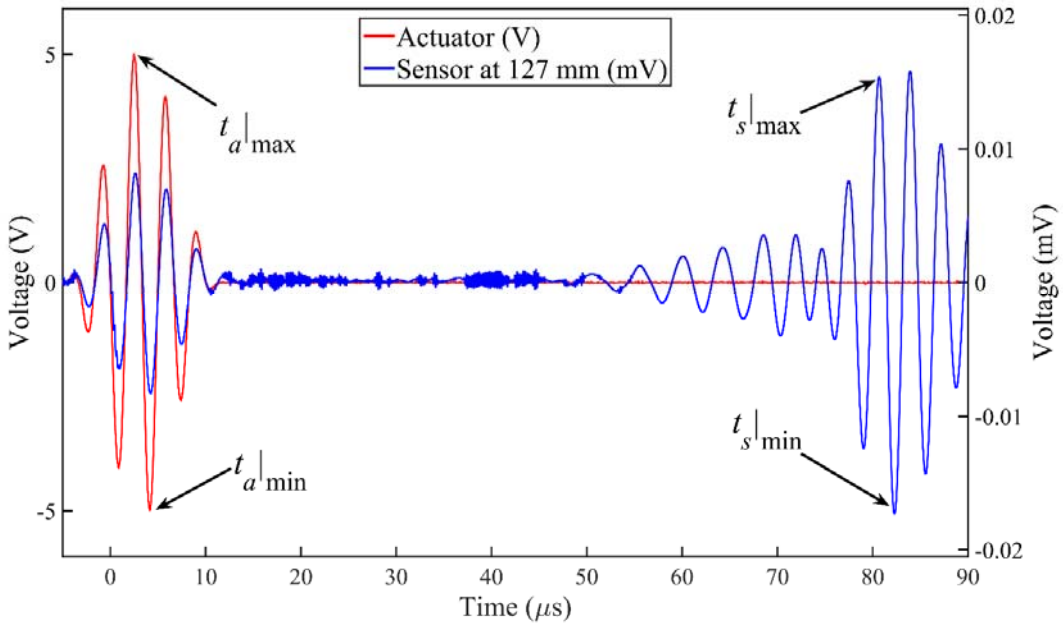

Figure 7. Actuation waveform (five-cycle, Hanning windowed sinusoidal toneburst signal with a center frequency of 300 kHz) and plate response from sensor located 127 mm from actuator.

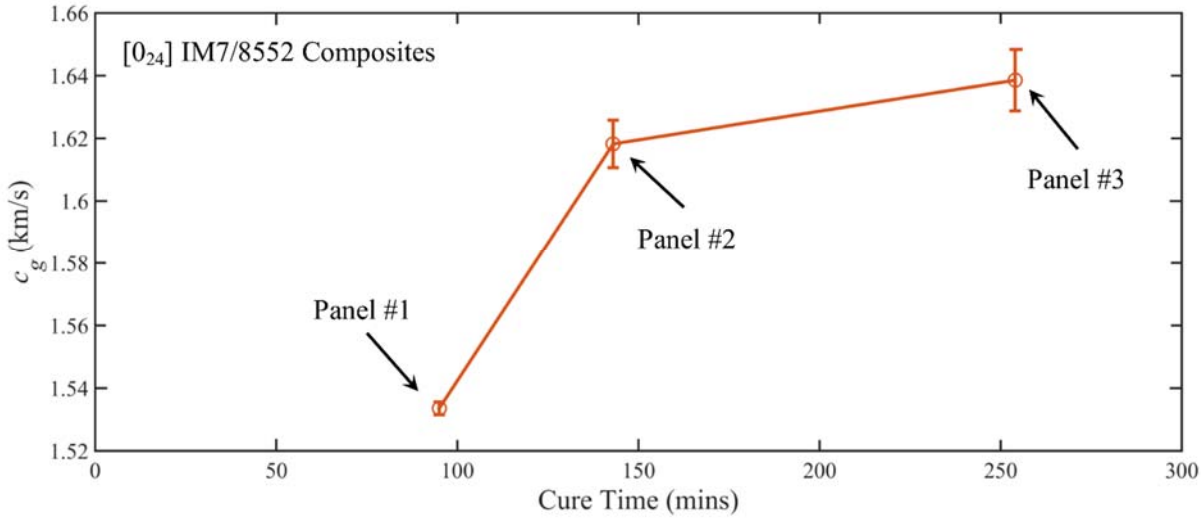

Figure 8. Group velocity normal to the fiber direction on each of three panels of varying final degrees of cure (Actuation with 300 kHz center frequency).

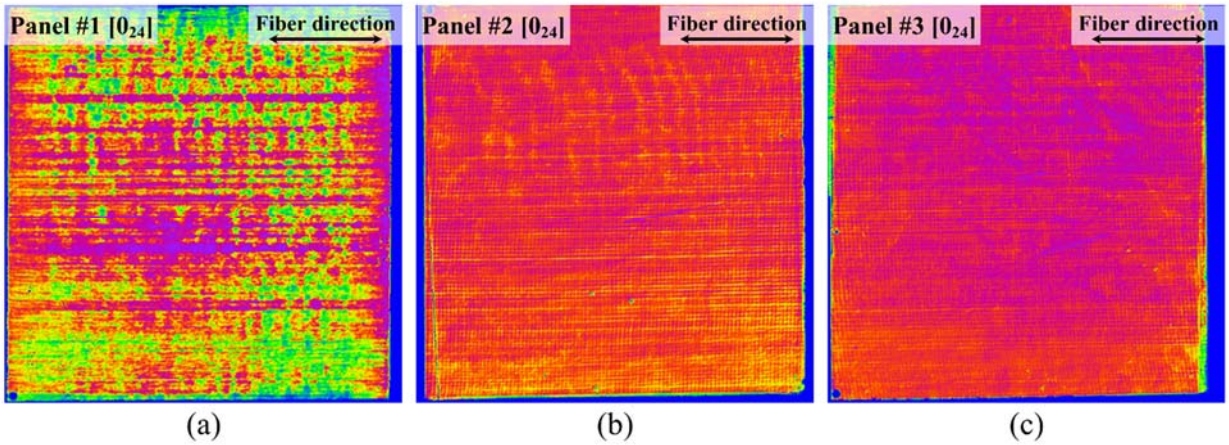

Figure 9. C-scan images of fabricated panels: (a) Panel #1, (b) Panel #2, and (c) Panel #3.

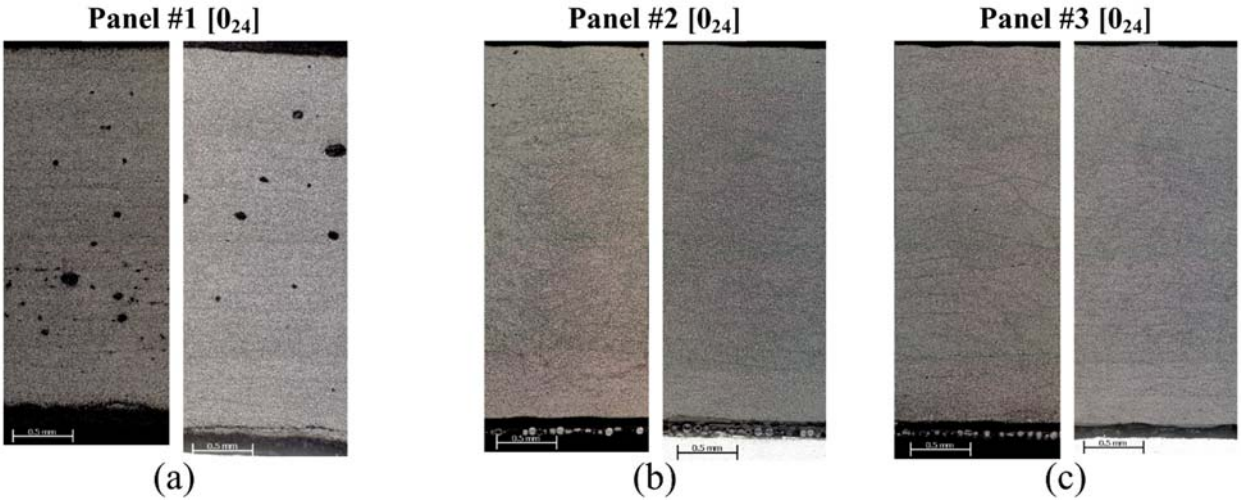

Figure 10. Micrographs at two locations in (a) Panel #1, (b) Panel #2, and (c) Panel #3.

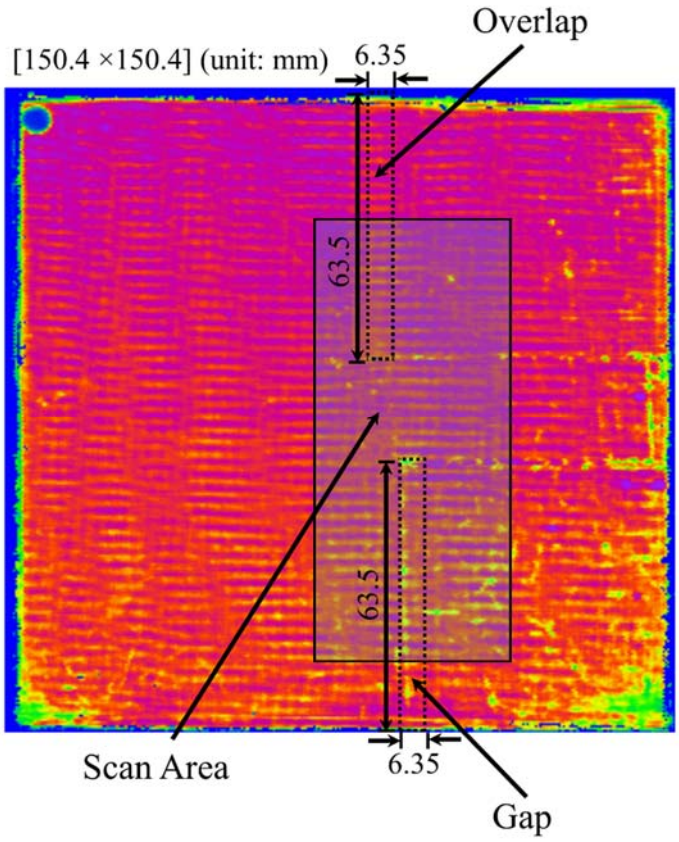

Figure 11. C-scan image of panel with intentionally introduced overlap and gap.

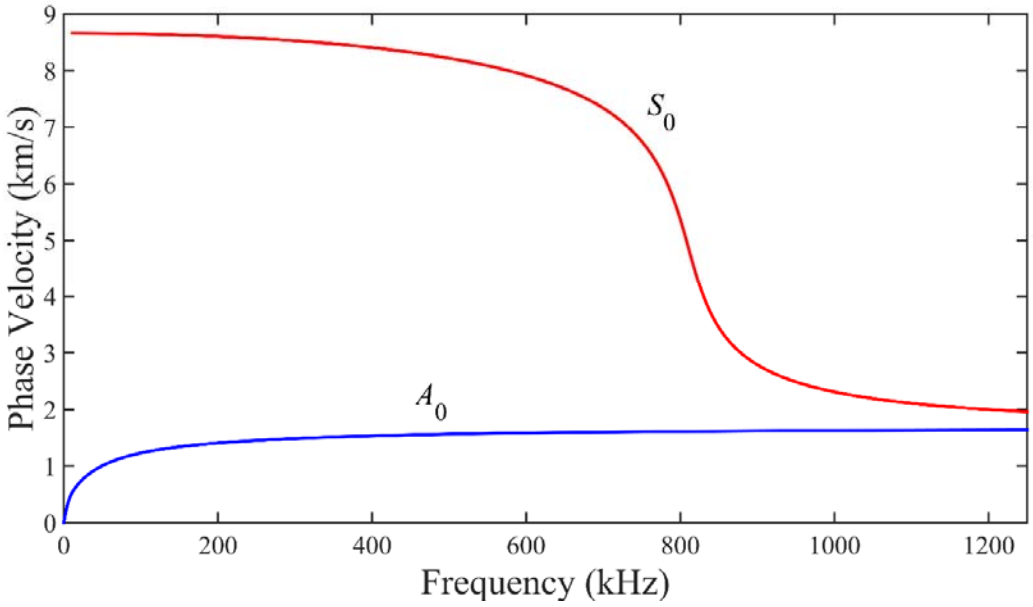

Figure 12. Phase velocity dispersion curve for the [0_4/90/90_2/90/0_4] composite plate.

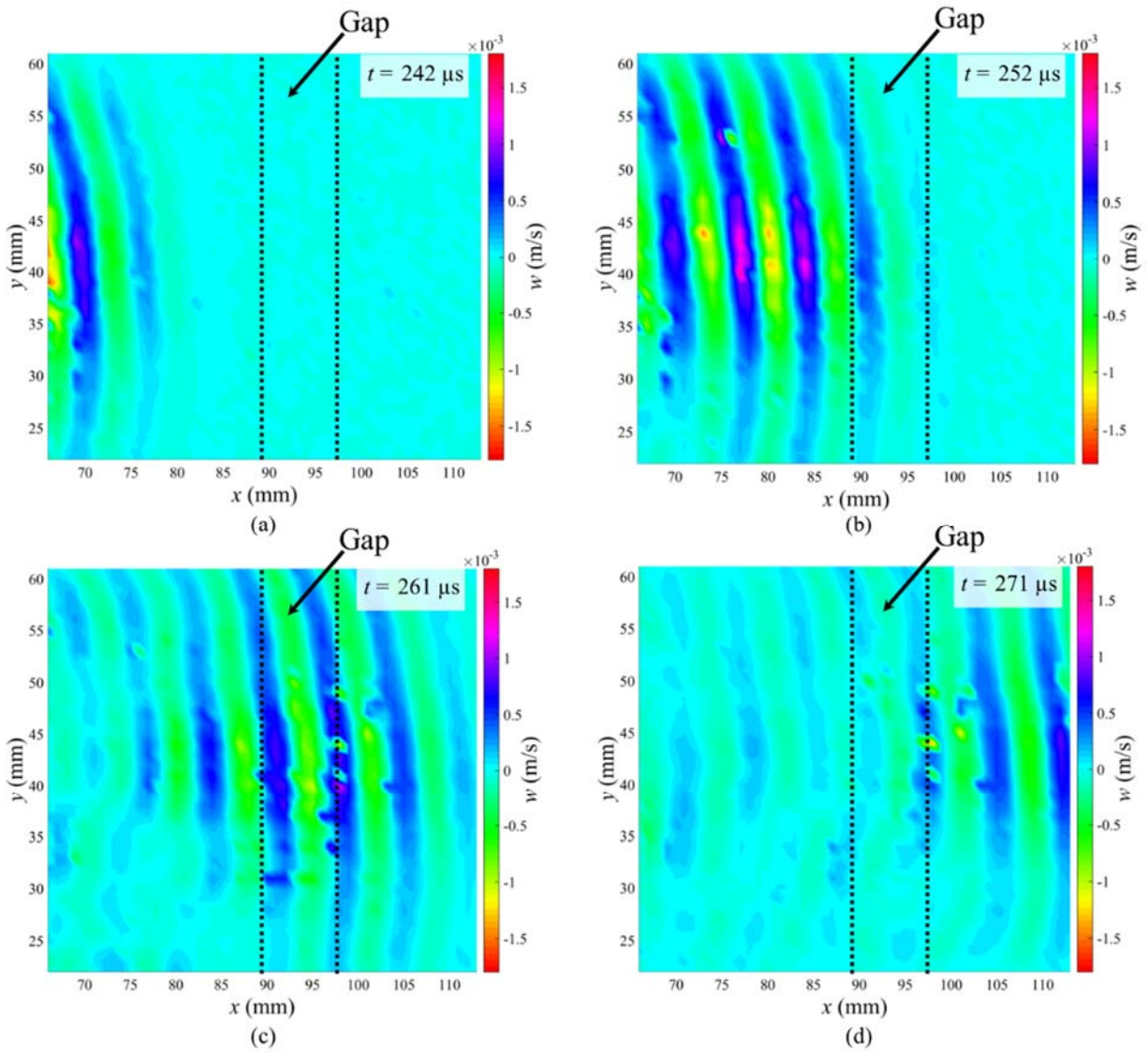

Figure 13. 2-D contour plots of the out-of-plane velocity, $w(x, y, t)$, of wavefield at times (a) 242 μs, (b) 252 μs, (c) 261 μs, and (d) 271 μs for the scan where the ACT is centered at y = 20 mm and on the left of the scan area.

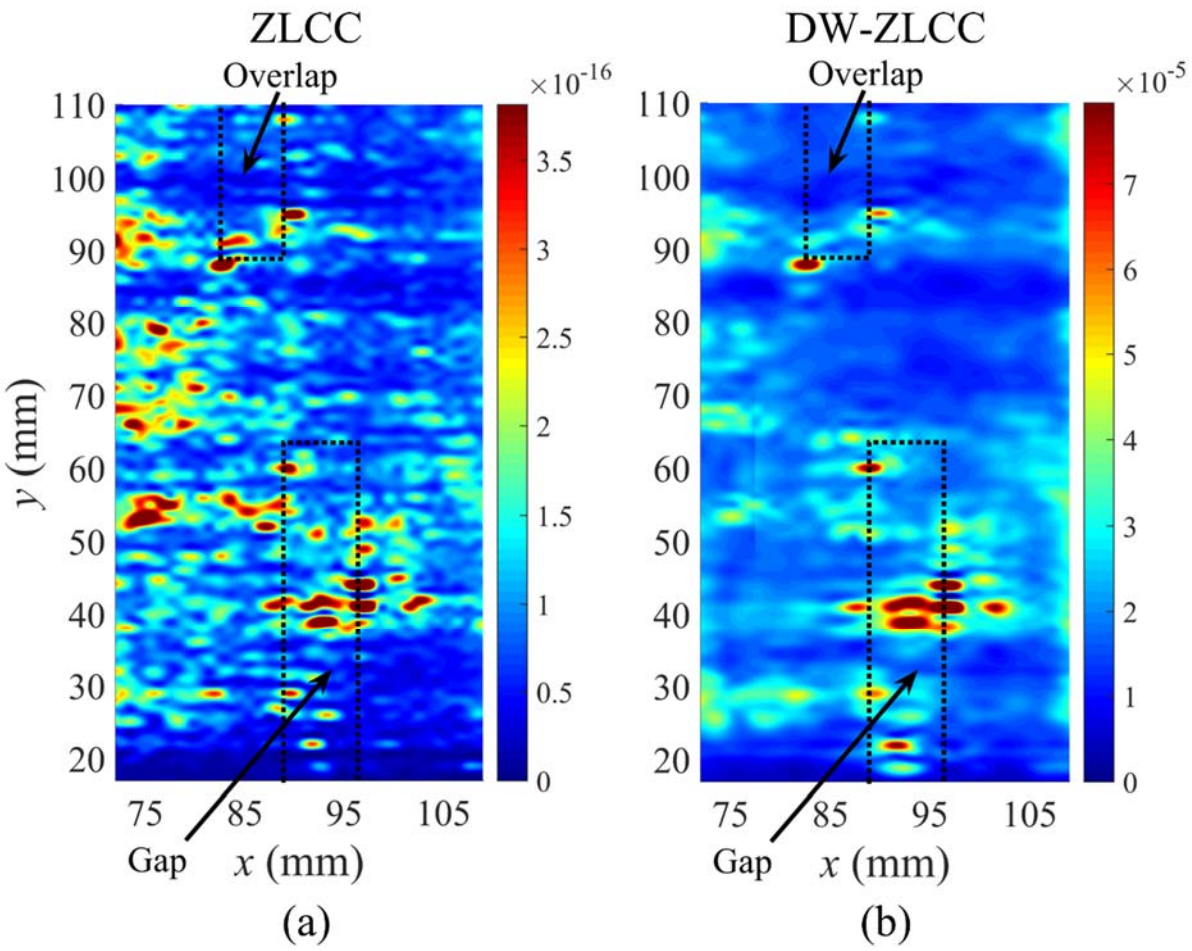

Figure 14. (a) ZLCC and (b) DW-ZLCC imaging condition [Gap (top) and overlap (bottom) locations are denoted by a dashed outline].